

Diffuse optical tomography with spectral constraints and wavelength optimization

Alper Corlu, Regine Choe, Turgut Durduran, Kijoon Lee, Martin Schweiger, Simon R. Arridge, Elizabeth M. C. Hillman, and Arjun G. Yodh

We present an algorithm that *explicitly* utilizes the wavelength dependence of tissue optical properties for diffuse optical tomography. We have previously shown that the method gives superior separation of absorption and scattering. Here the technique is described and tested in detail, and optimum wavelength sets for a broad range of chromophore combinations are discovered and analyzed. © 2005 Optical Society of America

OCIS codes: 170.3010, 170.3660, 170.3830, 170.5280, 170.6960, 100.3190.

1. Introduction

Diffuse optical tomography (DOT) is emerging as a means of deep-tissue optical imaging.^{1,2} DOT has a broad range of applications in optical breast imaging,^{3–10} functional brain spectroscopy and imaging,^{2,11–14} exercise medicine,^{15–18} and photodynamic therapy monitoring.^{19,20}

In a typical DOT system, light is injected into tissue and is then detected at other points on the tissue surface. Three measurement schemes are used for these measurements: time domain, frequency domain, and continuous wave (cw). Measurements are made in transmission, reflection, or both. Of these three measurement types, the cw method is the simplest, least expensive, and provides the fastest data collection. Nevertheless, widespread application of the cw method for DOT has been controversial. For example, it has been theoretically demonstrated that cw measurements lack the capability for separating absorption from scattering in the DOT image reconstruction.²¹ On the other hand, some researchers

have shown that this nonuniqueness problem of cw imaging can be minimized through preconditioning and regularization techniques.^{22–25}

In this paper we show that measurements at multiple wavelengths are the key for obtaining physiologically relevant tissue parameters with cw light. Until recently, commonly employed inverse methods calculated light absorption and scattering coefficients sequentially at each measurement wavelength and then decomposed the absorption data into contributions from various tissue chromophores and scattering components.

We present a new approach for extracting these tissue components. The multispectral method directly reconstructs tissue chromophore concentrations and Mie scattering factors by exploiting their *a priori* spectral properties.^{5,26–28} This new set of reconstructed variables is wavelength independent; hence data from all measurement wavelengths may be used simultaneously for reconstruction. Our approach effectively reduces the number of unknowns and produces a better-constrained inverse problem. We recently showed that this *a priori* spectral technique helps to overcome the nonuniqueness problem associated with cw imaging.²⁷

The remainder of this paper is structured as follows. In Sections 2 and 3 we provide details of the multispectral model for both the forward and inverse problems. We show explicitly how uniqueness can be achieved within the multispectral model and provide a criteria for choosing optimum wavelengths. In this paper we provide many more details compared with our previous short letter,²⁷ which largely summarized the theoretical results. In Section 4 we use this analysis to discover optimum wavelength distribu-

A. Corlu (corlua@dept.physics.upenn.edu), R. Choe, T. Durduran, K. Lee, and A. G. Yodh are with the Department of Physics and Astronomy, University of Pennsylvania, Philadelphia, Pennsylvania 19104. M. Schweiger and S. R. Arridge are with the Department of Computer Science, University College London, Gower Street, London WC1E 6BT, United Kingdom. E. M. C. Hillman is with the Martinos Center for Biomedical Imaging, Massachusetts General Hospital, Harvard Medical School, Building 149, 13th Street, Charlestown, Massachusetts 02129.

Received 26 July 2004; revised manuscript received 13 November 2004; accepted 15 November 2004.

0003-6935/05/112082-12\$15.00/0

© 2005 Optical Society of America

tions, and we investigate how different tissue chromophore and wavelength combinations affect these optimum wavelength sets. In Section 5 we discuss the feasibility of reconstructing scattering power with scattering prefactor and tissue chromophores. In Section 6 we discuss the generalization of our approach to frequency- and time-domain measurements. Finally, in Section 7 we apply the approach for three-dimensional (3D) reconstruction *in vivo*.

2. Multispectral Method

In this section we describe the multispectral model in detail. First, we define the forward problem in terms of multispectral parameters. We then formulate the inverse problem and provide two different frameworks for its solution.

A. Forward Problem

Light transport in tissue is well approximated as a diffusion process under certain conditions.² In the forward problem we are interested in calculating the light fluence rate, Φ , given some set of tissue optical properties. We use the photon diffusion equation in the frequency domain for this purpose, i.e.,

$$-\nabla \cdot D(\lambda) \nabla \phi(\lambda, \omega) + \left[\mu_a(\lambda) + \frac{i\omega}{v} \right] \phi(\lambda, \omega) = q_0(\lambda, \omega). \quad (1)$$

Here λ is the measurement wavelength, ω is the source-modulation frequency, v is the speed of light in the medium (assumed to be known), $\mu_a(\lambda)$ is the absorption coefficient, $D(\lambda)$ is the diffusion coefficient given approximately in terms of reduced scattering coefficient $\mu_s'(\lambda)$ as $1/(3\mu_s')$,^{29,30} and $q_0(\lambda, \omega)$ is the source term. For the solution of Eq. (1), we employ the Robin-type boundary condition

$$\phi + \frac{D d\phi}{\alpha d\hat{\mathbf{n}}} = 0, \quad (2)$$

where $\hat{\mathbf{n}}$ is the vector normal to the measurement boundary and α is related to the refractive-index mismatch at the boundary.³¹ Tissue optical properties $\mu_a(\lambda)$ and $\mu_s'(\lambda)$ must be known to solve the forward problem [Eq. (1)]. The multispectral model is based on the known wavelength dependence of tissue parameters such as chromophore concentrations C_l , scattering prefactor A , and scattering power b ; A and b are related to the size, index of refraction, and concentration of scatterers in tissue as well as to the index of refraction of the surrounding medium.^{32,33} The mapping from concentrations of the l th chromophore C_l to $\mu_a(\lambda)$ is made by use of the known absorption extinction coefficient, $\epsilon_l(\lambda)$, of the l th chromophore, i.e.

$$\mu_a(\lambda) = \sum_{l=1}^L \epsilon_l(\lambda) C_l. \quad (3)$$

Here we assume L total chromophores contribute to the absorption at wavelength λ . The relation for scattering is based on a simplified Mie scattering theory,^{32,33} i.e.,

$$\mu_s'(\lambda) = A\lambda^{-b}. \quad (4)$$

Given some initial distribution of C_l , A , and b in tissue, Eq. (3) and (4) can be used to obtain $\mu_a(\lambda)$ and $\mu_s'(\lambda)$. Once the mapping to optical parameters is done, the diffusion equation can be solved for the calculated fluence rate, Φ , by use of analytical or numerical methods. Tissue images are reconstructed by comparison of calculated fluence with the experimentally measured fluence, as discussed in Subsection 2.B.

B. Generalized Inverse Problem

We next reformulate the inverse problem that is appropriate to the multispectral model, focusing on nonlinear methods. We start with the Jacobian formulation. The Jacobian approach is common within the DOT community, since the same Jacobian matrix can be used in a single-step inversion scheme (i.e., the linear method).

In the Subsection 2.B.2 we outline a gradient-based framework that does not require a Jacobian matrix. This method is especially useful for systems with large numbers of source–detector pairs and large reconstruction domains wherein building and inverting the Jacobian matrix can be computationally difficult and even impossible owing to memory limitations. Although the computer simulations and *in vivo* results (Section 7) utilize this latter inversion framework, we still describe the Jacobian method to provide a better understanding of the concepts.

As discussed in Section 1, the traditional DOT inverse problem deals with reconstructing $\mu_a(\lambda)$ and $\mu_s'(\lambda)$ images for each measurement wavelength λ . These images are then converted to C_l , A , and b images by use of Eqs. (3) and (4). In the multispectral imaging approach, the goal is to obtain C_l , A , and b images directly. This requires some modifications to the image reconstruction formalism.

1. Jacobian Solver

Tissue chromophore concentrations C_l and scattering parameters A and b are wavelength independent. Therefore data acquired from all measurement wavelengths can be used simultaneously for inversion. Specifically, the inverse problem is defined as minimizing the objective function, χ^2 , a sum of “data mismatch” at each measurement wavelength, i.e.,

$$\chi^2 = \frac{1}{2} \sum_{n=1}^N \sum_{j=1}^S \sum_{i=1}^{M_j} [F_{j,i}(\lambda_n) - P_{j,i}(\lambda_n)]^2, \quad (5)$$

$$\chi^2 = \frac{1}{2} \mathbf{y}^T \mathbf{y}. \quad (6)$$

Here S is the total number of sources and M_j is the

number of detectors linked to source j , resulting in a total number of measurements $M_{\text{TOT}} = \sum_{j=1}^S M_j$. Measured and calculated fluence rates [log (fluence rate) in Rytov approximation³⁵] on the tissue boundary at wavelength λ_n are denoted by $F_{j,i}(\lambda_n)$ and $P_{j,i}(\lambda_n)$, respectively. \mathbf{y} is the residual data vector with $y_{j,i}(\lambda_n) = [F_{j,i}(\lambda_n) - P_{j,i}(\lambda_n)]$.

Letting \mathbf{x} represent either $\mathbf{C}_l(\mathbf{r})$, $\mathbf{A}(\mathbf{r})$, or $\mathbf{b}(\mathbf{r})$, we start with the Taylor expansion of $\chi^2(\mathbf{x})$ around some \mathbf{x}^0 up to second order in \mathbf{x} :

$$\chi^2(\mathbf{x}) = \chi^2(\mathbf{x}^0) + (\nabla\chi^2(\mathbf{x}^0))^T(\mathbf{x} - \mathbf{x}^0) + \frac{1}{2}(\mathbf{x} - \mathbf{x}^0)^T \mathbf{H}(\mathbf{x}^0)(\mathbf{x} - \mathbf{x}^0) + \dots, \quad (7)$$

where $\mathbf{H}_{ij} = \partial^2\chi^2/\partial x_i\partial x_j$ is the Hessian matrix.

Following Newton's method, we set the derivative $\partial\chi^2(\mathbf{x})/\partial x_k = 0$ for each k th component of vector \mathbf{x} and obtain the equality

$$0 = -\mathbf{y}^T \mathbf{J} + \frac{1}{2}[\Delta x^T(\mathbf{H}^T + \mathbf{H}) + 2\text{Diag}(\mathbf{H})\Delta \mathbf{x}]. \quad (8)$$

submatrix of size $M_{\text{TOT}} \times B$ and has the following structure:

$$\mathbf{J}_{\lambda_n}(\mathbf{x}) = \begin{bmatrix} \frac{\partial P_{1,1}(\lambda_n)}{\partial x_1} & \frac{\partial P_{1,1}(\lambda_n)}{\partial x_2} & \dots & \frac{\partial P_{1,1}(\lambda_n)}{\partial x_B} \\ \vdots & \vdots & \dots & \vdots \\ \frac{\partial P_{1,M_1}(\lambda_n)}{\partial x_1} & \frac{\partial P_{1,M_1}(\lambda_n)}{\partial x_2} & \dots & \frac{\partial P_{1,M_1}(\lambda_n)}{\partial x_B} \\ \vdots & \vdots & \dots & \vdots \\ \frac{\partial P_{j,i}(\lambda_n)}{\partial x_1} & \frac{\partial P_{j,i}(\lambda_n)}{\partial x_2} & \dots & \frac{\partial P_{j,i}(\lambda_n)}{\partial x_B} \\ \vdots & \vdots & \dots & \vdots \\ \frac{\partial P_{S,M_S}(\lambda_n)}{\partial x_1} & \frac{\partial P_{S,M_S}(\lambda_n)}{\partial x_2} & \dots & \frac{\partial P_{S,M_S}(\lambda_n)}{\partial x_B} \end{bmatrix}, \quad (11)$$

where x_k is the k th component of vector \mathbf{x} sampled at a basis of size B . The derivatives given in Eq. (11) can be related to derivatives with respect to absorption and scattering via the chain rule for variants of x_k :

$$\frac{\partial P_{j,i}(\lambda)}{\partial x_k} = \begin{cases} \frac{\partial \mu_a(\lambda)}{\partial C_{l,k}} \frac{\partial P_{j,i}(\lambda)}{\partial \mu_{a(k)}(\lambda)} = \epsilon_l(\lambda) \frac{\partial P_{j,i}(\lambda)}{\partial \mu_{a(k)}(\lambda)} & \text{if } x_k = C_{l,k} \text{ (} l\text{th tissue chromophore)} \\ \frac{\partial \mu_s'(\lambda)}{\partial A_k} \frac{\partial P_{j,i}(\lambda)}{\partial \mu_{s(k)}'(\lambda)} = \lambda^{-b_k} \frac{\partial P_{j,i}(\lambda)}{\partial \mu_{s(k)}'(\lambda)} & \text{if } x_k = A_k \text{ (scattering prefactor)} \\ \frac{\partial \mu_s'(\lambda)}{\partial b_k} \frac{\partial P_{j,i}(\lambda)}{\partial \mu_{s(k)}'(\lambda)} = -A_k \lambda^{-b_k} \ln(\lambda) \frac{\partial P_{j,i}(\lambda)}{\partial \mu_{s(k)}'(\lambda)} & \text{if } x_k = b_k \text{ (scattering power)} \end{cases}, \quad (12)$$

For cases in which no high spatial frequency information is expected to be recovered, the second-order terms can be omitted and the Hessian can be approximated as $\mathbf{H} \approx \mathbf{J}^T \mathbf{J}$. Hence, from Eq. (8), the following solution for the update vector ($\Delta \mathbf{x}$) is obtained:

$$\Delta \mathbf{x} = (\mathbf{J}^T \mathbf{J})^{-1} \mathbf{J}^T \mathbf{y}, \quad (9)$$

where $\Delta \mathbf{x} = (\mathbf{x} - \mathbf{x}^0)$ and \mathbf{J} is the Jacobian matrix with $\mathbf{J} = \partial P/\partial \mathbf{x}$. The structure of \mathbf{y} and \mathbf{J} are as follows:

$$\mathbf{y} = \begin{bmatrix} \mathbf{y}_{\lambda_1} \\ \mathbf{y}_{\lambda_2} \\ \vdots \\ \mathbf{y}_{\lambda_N} \end{bmatrix}, \quad \mathbf{J} = \begin{bmatrix} \mathbf{J}_{\lambda_1}(\mathbf{C}_1) & \mathbf{J}_{\lambda_1}(\mathbf{C}_2) & \dots & \mathbf{J}_{\lambda_1}(\mathbf{C}_L) & \mathbf{J}_{\lambda_1}(\mathbf{A}) & \mathbf{J}_{\lambda_1}(\mathbf{b}) \\ \mathbf{J}_{\lambda_2}(\mathbf{C}_1) & \mathbf{J}_{\lambda_2}(\mathbf{C}_2) & \dots & \mathbf{J}_{\lambda_2}(\mathbf{C}_L) & \mathbf{J}_{\lambda_2}(\mathbf{A}) & \mathbf{J}_{\lambda_2}(\mathbf{b}) \\ \vdots & \vdots & \dots & \vdots & \vdots & \vdots \\ \mathbf{J}_{\lambda_N}(\mathbf{C}_1) & \mathbf{J}_{\lambda_N}(\mathbf{C}_2) & \dots & \mathbf{J}_{\lambda_N}(\mathbf{C}_L) & \mathbf{J}_{\lambda_N}(\mathbf{A}) & \mathbf{J}_{\lambda_N}(\mathbf{b}) \end{bmatrix}. \quad (10)$$

Here \mathbf{y}_{λ_n} is the residual data vector of length M_{TOT} at the measurement wavelength λ_n . Each $\mathbf{J}_{\lambda_n}(\mathbf{x})$ is a

where

$$\frac{\partial P_{j,i}}{\partial \mu_{a(k)}} = -\frac{1}{\phi(\mathbf{r}_j, \mathbf{r}_i)} G(\mathbf{r}_k, \mathbf{r}_i) \phi(\mathbf{r}_j, \mathbf{r}_k), \quad (13)$$

$$\frac{\partial P_{j,i}}{\partial \mu_{s(k)}'} = 3D^2 \frac{1}{\phi(\mathbf{r}_j, \mathbf{r}_i)} \nabla G(\mathbf{r}_k, \mathbf{r}_i) \cdot \nabla \phi(\mathbf{r}_j, \mathbf{r}_k), \quad (14)$$

are given by the Rytov approximation, with $G(\mathbf{r}_k, \mathbf{r}_i)$

being the adjoint solution at basis point \mathbf{r}_k for detector location \mathbf{r}_i .^{34,35}

The update vector $\Delta \mathbf{x}$ found at the end of the linearization step [Eq. (9)] is added to the initial guess \mathbf{x}^0 to reconstruct an updated image. This process can be repeated iteratively, giving a solution $\mathbf{x}^{t+1} = \mathbf{x}^t + \Delta \mathbf{x}^t$ at the $(t + 1)$ th iteration, where $\Delta \mathbf{x}^t$ is obtained from Eq. (9) with $\mathbf{J} = \mathbf{J}(\mathbf{x}^t)$.

2. Gradient-Based Scheme

This approach uses the gradient of the objective function to generate a minimum search direction. Calculation of the gradient vector $\nabla \chi^2(\mathbf{x})$ is straightforward. The k th component is

$$\frac{\partial \chi^2}{\partial x_k} = \sum_{n=1}^N \sum_{j=1}^S \sum_{i=1}^{M_j} [F_{j,i}(\lambda_n) - P_{j,i}(\lambda_n)] \left[-\frac{\partial P_{j,i}(\lambda_n)}{\partial x_k} \right], \quad (15)$$

where $\partial P_{j,i}(\lambda_n)/\partial x_k$ is given in Eq. (12). The key reason to employ this method is that the adjoint solution G in Eqs. (13) and (14) is replaced by the solution for the weighted sum of all detectors, where the weighting is the residual (\mathbf{y}), which can be computed directly by the forward solver, without the computational and memory overhead of computing \mathbf{J} .

Once the gradient vector is computed, any gradient-based generic algorithm can be applied to find the minimum of the objective function. In this study we consider nonlinear conjugate gradients with the Polak–Ribière method. The details of the algorithm can be found elsewhere.^{36,37}

3. Nonuniqueness in cw and Multispectral Method

In the case of cw measurements, it has been shown that different sets of absorption and scattering parameters can yield identical data.²¹ cw DOT inversions have cross talk between absorption and scattering. In this section we show how this nonuniqueness problem inherent in cw DOT can be overcome, provided the multispectral approach is used with the correct measurement wavelengths.²⁷ The choice of wavelengths is based on two considerations, i.e., the separation of absorption from scattering (nonuniqueness) and the separation of absorption chromophores from one another.

We start with the nonuniqueness concept as demonstrated by Arridge *et al.*²¹ The diffusion Eq. (1) is first simplified to a Helmholtz-type equation with the change of variables $\gamma^2 = D$ and $\Psi = \gamma\Phi$ and takes the form

$$-\nabla^2 \Psi(\omega) + \eta(\omega)\Psi(\omega) = \frac{q_0(\omega)}{\gamma}, \quad (16)$$

where $\eta = \eta_0 + i\omega\xi$, with

$$\eta_0 = \left(\frac{\nabla^2 \gamma}{\gamma} \right) + \frac{\mu_a}{\gamma^2}, \quad \xi = \frac{1}{v\gamma^2}. \quad (17)$$

Two conditions must be met to have two sets of samples (D, μ_a) and $(\tilde{D}, \tilde{\mu}_a)$ that produce the same

solution Ψ . First, $\tilde{\eta}(\omega)$ must be equal to $\eta(\omega)$ everywhere in the solution domain. Second, $\tilde{D} = D$ everywhere within the source layer.²¹

Any different set \tilde{D} has a different $\gamma^2 = \tilde{D}$, and hence a different $\xi = 1/v\gamma^2$. In general this violates the first condition given above, i.e., $\tilde{\eta}(\omega) = \eta(\omega)$. However, for $\omega = 0$ (cw case), η reduces to η_0 . In this case it becomes possible²¹ to find some $\Delta\mu_a$, given an arbitrary function ΔD such that

$$\tilde{D} = D + \Delta D, \quad \tilde{\mu}_a = \mu_a + \Delta\mu_a. \quad (18)$$

The resulting set $(\tilde{D}, \tilde{\mu}_a)$ satisfies the two conditions and produces an identical data set, as explicitly shown in Ref. 21. Since infinitely many arbitrary choices for ΔD exist, this result states that the inverse solver is likely to introduce cross talk between absorption and scattering when the measurement type is cw.

We now look into the nonuniqueness problem in the multispectral method framework. We first derive analogous conditions where the parameters D, μ_a are replaced by C_l, A, b . We next extend these conditions to multiple wavelengths.

Assume there exists another set $\tilde{b}, \tilde{A}, \tilde{C}_l$ with $\tilde{b} = b, \tilde{A} = A + \Delta A, \tilde{C}_l = C_l + \Delta C_l$. Here for practical reasons we do not regard b as an unknown. Instead, we assume it is spatially constant and known, i.e., $b(r) = b$. These two sets yield identical data provided the conditions given earlier are fulfilled. Given the arbitrary function ΔA (zero within $1/\mu_s'$ of the boundary), the first condition ($\tilde{\eta}_0 = \eta_0$) can be rewritten in terms of the new multispectral parameters as

$$\frac{1}{h(\lambda^b, \tilde{A})} \sum_l \frac{\epsilon_l(\lambda)}{\lambda^b} \left(\frac{\Delta A}{\tilde{A}} C_l + \Delta C_l \right) = 1, \quad (19)$$

where

$$h(\lambda^b, \tilde{A}) = \frac{1}{3\tilde{A}} \left(\frac{\nabla^2 \sqrt{\lambda^b/3A}}{\sqrt{\lambda^b/3A}} - \frac{\nabla^2 \sqrt{\lambda^b/3\tilde{A}}}{\sqrt{\lambda^b/3\tilde{A}}} \right). \quad (20)$$

Since $b(r)$ is assumed to be constant, $h(\lambda^b, \tilde{A})$ reduces to

$$h(\tilde{A}) = \frac{1}{3\tilde{A}} \left(\frac{\nabla^2 \sqrt{1/3A}}{\sqrt{1/3A}} - \frac{\nabla^2 \sqrt{1/3\tilde{A}}}{\sqrt{1/3\tilde{A}}} \right). \quad (21)$$

Equation (19) simply restates the nonuniqueness criterion in terms of the wavelength-independent variables C_l, A , and b .

So far we have limited our analysis to a single wavelength. The dramatic improvement of the multispectral method comes from using all measurement wavelengths *simultaneously*.

We now investigate the unlikelihood that two dif-

ferent parameter sets are capable of producing identical data simultaneously at all the measurement wavelengths. Suppose there are N measurement wavelengths and L chromophores (C_i), then the non-uniqueness condition becomes a matrix equality in which each row represents Eq. (19) for the wavelength (λ_n):

$$\begin{bmatrix} \epsilon_1(\lambda_1) & \epsilon_2(\lambda_1) & \dots & \epsilon_L(\lambda_1) \\ \lambda_1^b & \lambda_1^b & \dots & \lambda_1^b \\ \vdots & \vdots & \ddots & \vdots \\ \epsilon_1(\lambda_N) & \epsilon_2(\lambda_N) & \dots & \epsilon_L(\lambda_N) \\ \lambda_N^b & \lambda_N^b & \dots & \lambda_N^b \end{bmatrix} \times \left(\frac{\Delta A}{\tilde{A}h(\tilde{A})} \begin{bmatrix} C_1 \\ \vdots \\ C_L \end{bmatrix} + \frac{1}{h(\tilde{A})} \begin{bmatrix} \Delta C_1 \\ \vdots \\ \Delta C_L \end{bmatrix} \right) = \begin{bmatrix} 1 \\ \vdots \\ 1 \end{bmatrix}, \quad (22)$$

$$\mathbf{E}\mathbf{w} = \mathbf{1}. \quad (23)$$

Here \mathbf{E} denotes the wavelength-dependent matrix. The inverse problem has nonunique solutions if $\mathbf{E}\mathbf{w}$ is equal or very close to $\mathbf{1}$. Therefore the choice of \mathbf{E} , and ergo the wavelengths used, affects the reconstruction. The desired wavelengths form a matrix \mathbf{E} such that the distance between the closest solution to Eq. (22) and the vector $\mathbf{1}$ is *maximized*. The closest solution is given in a least-squares sense as $\mathbf{w}_o = (\mathbf{E}^T\mathbf{E})^{-1}\mathbf{E}^T\mathbf{1}$,³⁸ and the residual norm $R = \|\mathbf{1} - \mathbf{E}\mathbf{w}_o\|$ can be interpreted as the distinguishability parameter. The closer R is to zero, the closer \mathbf{w}_o will be to fulfilling the conditions for nonuniqueness. Wavelength choices that maximize R define our first criterion for selecting optimal wavelengths.

We next consider distinguishing chromophore concentrations among themselves. Equation (3) can be written in a matrix form for N wavelengths; $\boldsymbol{\mu}_a(\boldsymbol{\lambda}) = \boldsymbol{\epsilon}\mathbf{C}$, i.e.,

$$\begin{bmatrix} \mu_a(\lambda_1) \\ \vdots \\ \mu_a(\lambda_N) \end{bmatrix} = \begin{bmatrix} \epsilon_1(\lambda_1) & \dots & \epsilon_L(\lambda_1) \\ \vdots & \ddots & \vdots \\ \epsilon_1(\lambda_N) & \dots & \epsilon_L(\lambda_N) \end{bmatrix} \begin{bmatrix} C_1 \\ \vdots \\ C_L \end{bmatrix}. \quad (24)$$

When the matrix given in Eq. (24) has smooth singular-value distribution, we expect each chromophore to make similar contributions to absorption. The condition number $\kappa(\boldsymbol{\epsilon})$ can be used as a measure of the smoothness of $\boldsymbol{\epsilon}$. It is the ratio of the maximum to the minimum singular value. When κ is small, measurements have equal sensitivity to each chromophore; hence the cross talk within the absorption chromophores is minimized. Wavelength choices that *minimize* κ define our second criterion for selecting optimal wavelengths.

We have previously shown²⁷ how certain wavelength choices would affect the results with computer simulations by using three chromophores oxyhemoglobin, deoxyhemoglobin, and water as the main absorbers. Here we present similar simulations with

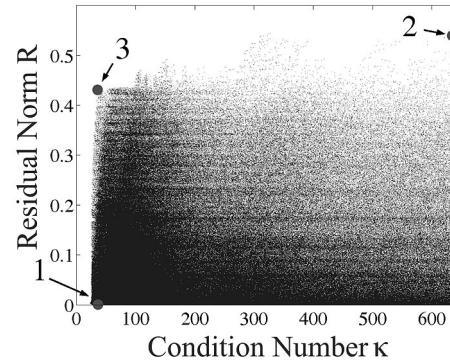


Fig. 1. Each point represents a set of five wavelengths. Residual norm, R , and condition number, κ , of each set are calculated for four chromophores HbO₂, HbR, H₂O, and lipid as described in Section 3. Points 1, 2, and 3 are selected as extreme points with high and low R and κ values.

the important additional tissue chromophore: lipid. Lipid is an important absorber in tissue, which has, for example, been shown to be correlated with breast physiology.⁴

For a medium with $L = 4$ absorption chromophores taken as oxyhemoglobin (HbO₂), deoxyhemoglobin (HbR), water (H₂O), and lipid, at least $N = 5$ wavelengths are required when the scattering prefactor A is also allowed to vary. Each set of five wavelengths has some value for residual norm R and condition number κ , given the extinction coefficients³⁹ and the scattering power b . Figure 1 shows the scatter plot of R and κ values computed with four chromophores and five wavelengths with the scattering power $b = 1.3$.⁵ The wavelengths were chosen from the 650 – 930-nm range (based on signal-to-noise calculations for 6-cm optode separations in a transmission geometry), spaced in 6-nm intervals. We consider three sets from different regions of Fig. 1: The first set is from low values of R and κ , the second set from high values of R and κ , and the third set from high values of R and low values of κ . These wavelength sets are tabulated in Table 1 with their corresponding R and κ values. Based on our analysis in Section 3, we expect the third set to be the optimal set.

To clearly see the effects of R and κ on our choice of wavelengths, we have simulated two different circular two-dimensional (2D) media with similar geometry, but one with an extra scattering inhomogeneity. Figure 2 shows the geometries of target media used in our simulations. Both media are 7 cm in diameter with 1.6-cm objects embedded in a homogeneous background. The first medium [Fig. 2(a)] is composed of four objects with different absorption perturba-

Table 1. Wavelength Sets Chosen from Fig. 1 and the Corresponding Condition Numbers (κ) and Residual Norms (R)

Set	Wavelengths (nm)	κ	R
1	740, 788, 866, 902, 926	36.5	4.5×10^{-6}
2	650, 700, 716, 860, 890	634.0	5.4×10^{-1}
3	650, 716, 866, 914, 930	36.4	4.3×10^{-1}

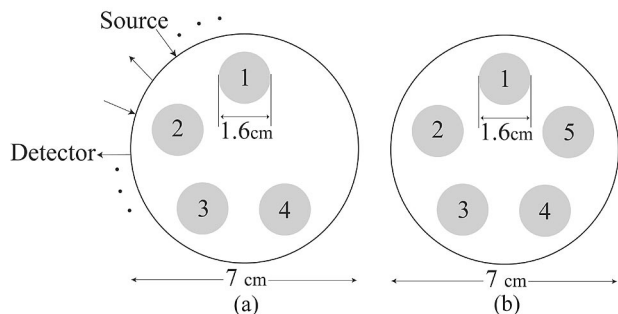


Fig. 2. Geometry of the circular media used in the simulations. Thirty-two source–detector pairs are equally spaced along the circumference. The first medium (a) has four absorbing objects, and the second medium (b) includes an additional scattering object. Both media are 7 cm in diameter with objects of 1.6 cm in diameter.

tions owing to different chromophores. The second medium [Fig. 2(b)] has an additional fifth object with a scattering inhomogeneity owing to scattering prefactor A . Table 2 lists the concentrations and the scattering prefactor values with corresponding object locations. Background values correspond to $\mu_a = 0.06 \text{ cm}^{-1}$ and $\mu_s' = 7.6 \text{ cm}^{-1}$ at $\lambda = 800 \text{ nm}$.⁵

A finite-element⁴⁰ mesh with 4159 nodes was used to generate forward cw data at 32 source and detector positions equally spaced along the circumference. To imitate real data acquisition, 1% random Gaussian noise was added to the data. Images of absorption chromophores and scattering prefactor A were reconstructed with the method discussed in Subsection 2.B.2.

Figure 3 shows the reconstructed chromophore images simulated in the first medium. Each row corresponds to a different chromophore with the target locations shown in the first column, and the subsequent columns display the reconstructed images for wavelength sets 1, 2, and 3. Sets 1 and 3 give similar images, however set 2, due to its high κ value, fails to distinguish between H_2O and lipid.

Reconstruction results for the second target medium wherein a scattering (fifth) object was embedded are shown in Fig. 4. The first set with the addition of a scattering object yields a low contrast (15- μM peak) for the HbR image and shows some cross talk between absorption chromophores (not present in absence of scattering; see Fig. 3). The second set has reduced scattering cross talk with respect to first set

Table 2. Chromophore Concentration and Scattering Coefficient Prefactor Values of the Background and the Test Objects

Location	HbO ₂ (μM)	HbR (μM)	H ₂ O (%)	Lipid (%)	A ($10^{-6b} \text{ mm}^{b-1}$)
Background	20	10	27	25	4500
Object 1	40	10	27	25	4500
Object 2	20	20	27	25	4500
Object 3	20	10	54	25	4500
Object 4	20	10	27	50	4500
Object 5	20	10	27	25	9000

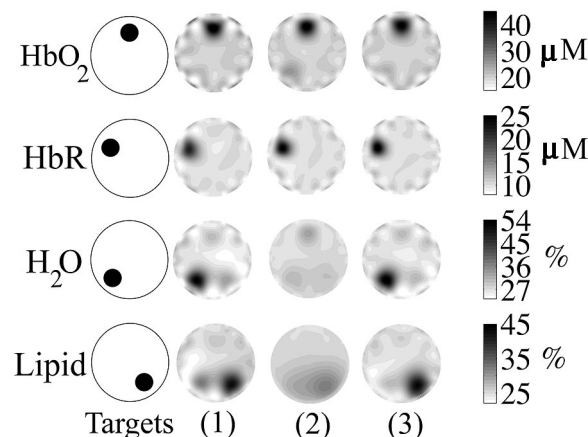


Fig. 3. Image reconstruction results of the first medium. Images of chromophores HbO₂, HbR, H₂O, and lipid are shown in consecutive rows. The leftmost column shows the expected target object locations, and the rest of the columns display the reconstructed images of chromophores for sets 1, 2, and 3.

but still exhibits very low contrast for the H_2O image. The third set yields the best contrast and localization for all five target objects, which is consistent with our expectation of the optimum wavelength set to have high R and low κ values. The wavelengths in the third set were also used with the conventional DOT image reconstruction scheme, wherein absorption and scattering at each wavelength are obtained first and are then decomposed into chromophore concentrations images as shown in the last column of Fig. 4. The scattering cross talk in the chromophore images clearly demonstrates the superiority of the multispectral method over the traditional DOT method. (Note that no regularization or matrix scaling techniques were employed in any of the image reconstructions.)

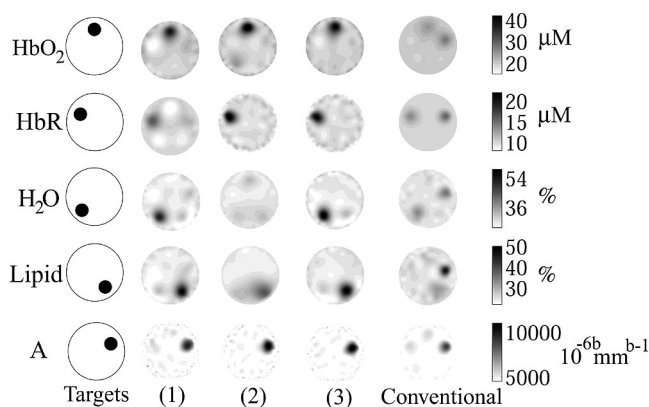


Fig. 4. Reconstructed images for the second target medium. Target images of HbO₂, HbR, H₂O, lipid, and A are shown in the first, second, third, fourth, and fifth rows of the leftmost column, respectively. The images shown in the second to fourth columns are reconstructed with the multispectral method for sets 1, 2, and 3. The images in the rightmost column are obtained with conventional DOT image reconstruction with the wavelengths used in set 3.

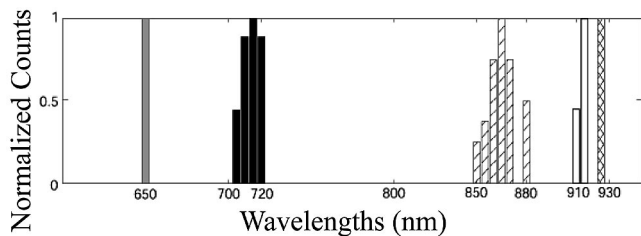


Fig. 5. Histogram of optimum wavelength distributions with five wavelengths and four chromophores (HbO₂, HbR, H₂O, lipid). Each wavelength count (distinguished by different patterns) in a set is normalized for ease of demonstration.

4. Optimum Wavelength Distributions

In this section we examine wavelength distributions in Fig. 1 more closely by using histograms. We first consider optimum sets for the case with four absorption chromophores (HbO₂, HbR, H₂O, lipid) and five measurement wavelengths. Notice that scattering is implicitly included; i.e., the R and κ values are calculated based on absorption chromophores to be extracted and the number of measurement wavelengths. We define the optimum wavelength sets as the sets (points) in the neighborhood of set 3 in Fig. 1. We choose the neighborhood of set 3 as the points falling in a somewhat arbitrary range defined to be $R \geq 0.415$ and $\kappa \leq 40.0$. Note that each point is a set of five wavelengths. The histogram obtained by counting the number of repetitions for each of the five wavelengths separately (see Fig. 5) reveals that each wavelength choice tends to cluster around particular central wavelengths. The optimum five-wavelength sets fall in the range 650 ± 3 , 710 ± 10 , 865 ± 15 , 912 ± 4 , and 928 ± 4 nm. Any arbitrary combination of these five wavelengths stays in the same neighborhood of R , κ values.

We next examine how the histograms change with the different types of chromophores and the different numbers of wavelengths used. Suppose that there are only two primary absorption chromophores, i.e., oxyhemoglobin (HbO₂) and deoxyhemoglobin (HbR). $R - \kappa$ distributions similar to those in Fig. 1 are obtained for different numbers of wavelengths $N = 3, 4, 5$. Each distribution (not shown) has an optimum set with high R and low κ values. The histograms of the optimum wavelength sets are shown in Fig. 6. With three wavelengths (the minimum number needed $N > L = 2$), the optimum sets are 650 ± 2 , 716 ± 4 , and 902 ± 16 , as seen in Fig. 6(a). Figures 6(b) and 6(c) show that the addition of the fourth and fifth wavelengths does not provide any new group, but rather broadens the second wavelength range from 716 ± 4 to 720 ± 16 nm, and that the last wavelength range shifts slightly from 902 ± 16 to 896 ± 30 nm. The data suggest that when the absorption chromophores are only HbO₂ and HbR, the optimum wavelength formulation developed gives an optimum set with three rather distinct wavelengths no matter how many wavelengths are used to get R and κ .

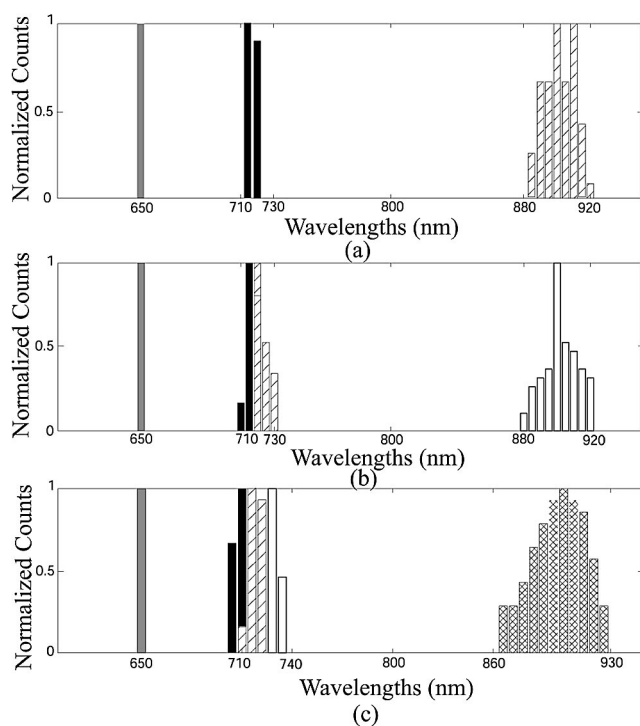


Fig. 6. Histograms for the optimum wavelength sets obtained with two absorption chromophores (HbO₂ and HbR) for different numbers of wavelengths N : (a) $N = 3$, (b) $N = 4$, (c) $N = 5$.

We performed a similar analysis this time with three chromophores [oxyhemoglobin (HbO₂), deoxyhemoglobin (HbR), and water (H₂O)] and obtained the histograms shown in Fig. 7. In the case of four wavelengths we obtain the histogram in Fig. 7(a), which shows that the optimum sets fall in the ranges of 650 ± 2 , 722 ± 10 , 884 ± 24 , and 930 ± 2 nm, as reported in our previous letter.²⁷ Increasing the number of wavelengths from four [Fig. 7(a)] to five [Fig. 7(b)] broadens the second wavelength range from 722 ± 10 to 720 ± 20 nm, but it also shifts the center of the third wavelength distribution from 884 to 836 nm. When we use six wavelengths [Fig. 7(c)], an additional peak in the distribution occurs centered at 880 nm. These last histograms show that, with three chromophores HbO₂, HbR, and H₂O, when we exceed four wavelengths, the $R - \kappa$ maps provide a quantitatively new set, provided more than one measurement wavelength is to be selected from the 720 ± 15 -nm range.

5. Scattering Prefactor A and Power b

The optimum wavelength analysis discussed in Section 3 assumed a homogeneous and fixed value for the scattering power b . This assumption makes it possible to easily compute the matrix in Eq. (22) numerically. However, the scattering power b may not be homogeneous in tissue. It is therefore necessary to quantify the error induced by this assumption.

So far we have used the simplified Mie theory to express the reduced scattering coefficient as $\mu_s' = A\lambda^{-b}$.³² A more general way of writing the scatter-

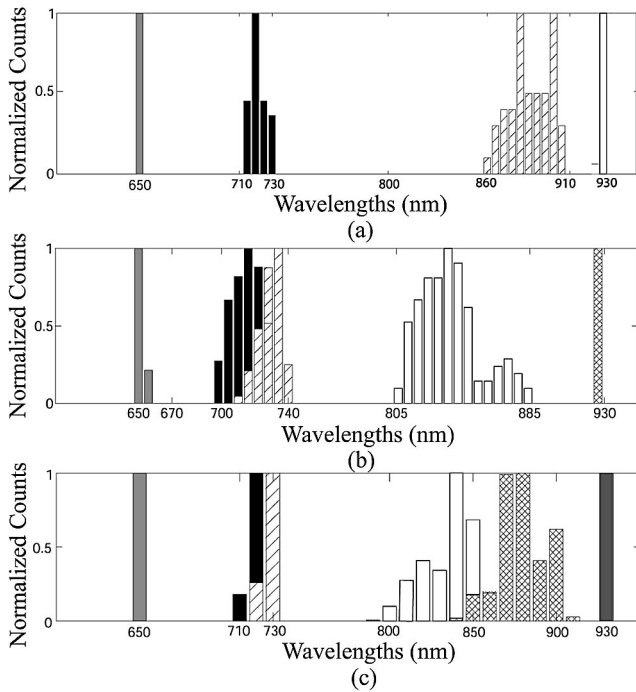


Fig. 7. Histograms for the optimum wavelength sets obtained with three absorption chromophores (HbO₂, HbR, and H₂O) for different numbers of wavelengths N : (a) $N = 4$, (b) $N = 5$, (c) $N = 6$.

ing coefficient is³³

$$\mu_s' = a(2\pi\rho n_m)^b \lambda^{-b}, \quad (25)$$

where a is proportional to the density of the scattering centers, ρ is the radius of the scatterers, and n_m is the index of refraction of the medium. The value of b varies between 0.37 and 4 as the radius of scatterers changes from 1 to 0.05 μm .³³ Equation (25) suggests that separate measurements of A and b are needed to quantify the scattering size and density of the scatterers in tissue.

A simulation of three scattering objects with different target A and b images is shown in Fig. 8. To have a good fit, a large number of wavelengths ($N = 15$) sampled from the 650–930-nm range at 20-nm intervals were used. In the reconstructions we found that the scattering prefactor (A) and power (b) exhibited strong cross talk; typically b tends to be updated rather than A . The cross talk between A and b can be attributed to valleys appearing in the contour plot of the log of the error function, as seen in Fig. 9(a). Here we define the error function as

$$E(A, b) = \sum_{i=1}^{i=N} \{\log(A\lambda_i^{-b}) - \log[\mu_s'(A_o, b_o, \lambda_i)]\}^2, \quad (26)$$

where $A_o = 9000$ and $b_o = 1.3$ are chosen to give $\mu_s'(650 \text{ nm}) = 19.8 \text{ cm}^{-1}$ and $\mu_s'(930 \text{ nm}) = 12.5 \text{ cm}^{-1}$, respectively. The value of E changes more rapidly with b , as shown in Fig. 9(a), thus explaining why

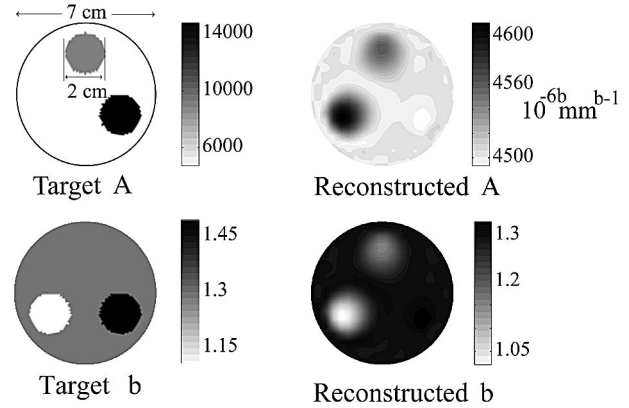


Fig. 8. Target and reconstructed images of A and b obtained with the multispectral method with 15 wavelengths sampled from the 650–930-nm range at 20-nm intervals.

the scattering perturbations are compensated mainly by updates in b .

We now introduce a new set of variables that yields a better scaled problem. Let $\zeta = \log(A) + r b$ and $\beta = b/t$. Here we set

$$r = -\frac{1}{N} \sum_{i=1}^{i=N} \log(\lambda_i), \quad t = N \left[N \sum_{i=1}^{i=N} \log^2(\lambda_i) - (rN)^2 \right]^{-1/2} \quad (27)$$

so that the resulting error function $E(\zeta, \beta)$ written in terms of ζ and β takes the form of a noninteracting function; i.e., there are no cross terms in the expansion:

$$\begin{aligned} E(\zeta, \beta) &= \sum_{i=1}^{i=N} \{ \zeta - rt\beta - t\beta \log(\lambda_i) - \log[\mu_s'(A_o, b_o, \lambda_i)] \}^2 \\ &= N\zeta^2 + N\beta^2 - \zeta \left\{ 2 \sum_{i=1}^{i=N} \log[\mu_s'(A_o, b_o, \lambda_i)] \right\} \\ &\quad + \beta \left\{ 2rt \sum_{i=1}^{i=N} \log[\mu_s'(A_o, b_o, \lambda_i)] \right. \\ &\quad \left. + 2t \sum_{i=1}^{i=N} \log(\lambda_i) \log[\mu_s'(A_o, b_o, \lambda_i)] \right\} \\ &\quad + \sum_{i=1}^{i=N} \log^2[\mu_s'(A_o, b_o, \lambda_i)]. \end{aligned} \quad (28)$$

The circular contours shown in Fig. 9(b) illustrate the improvement in scaling achieved with this change of variables.

Figures 10(a) and 10(b) shows the reconstructed images of A and b , using the new set of variables ζ and β in the inversion. The scattering prefactor and power images are superior to those obtained without scaling. The conventional A , b images obtained by fitting $\mu_s'(\lambda)$ (reconstructed at each wavelength separately) to $A\lambda^{-b}$ are also shown for comparison in Figs. 10(c) and 10(d). The fitting process in the conventional case utilized the Nelder Mead simplex method implemented in the MATLAB function `fminsearch`. However, simulations (results not shown)

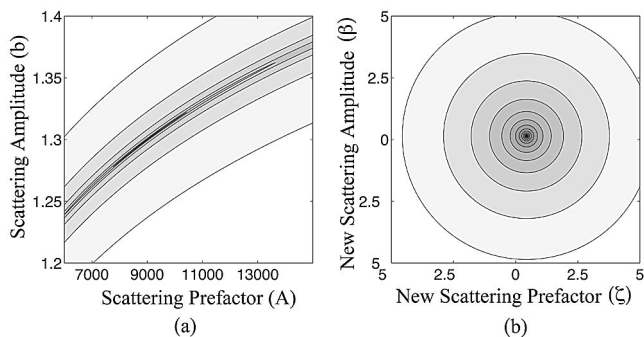


Fig. 9. Contour plots of the log of the error functions. (a) $E(A, b)$ is poorly scaled, as demonstrated by the presence of narrow contour valleys. The global minimum is located at $A_0 = 9000$ and $b_0 = 1.3$. (b) The same error function expressed in terms of ζ and β has a well-defined minimum ($\zeta_0 = 0.44$, $\beta_0 = 0.14$), with circular contours illustrating the improvement in scaling.

with five objects [as in Fig. 2(b), wherein we let A , b or ζ , β vary] exhibited convergence problems for the absorption chromophore concentrations, and we were unable to reliably reconstruct A and b .

In summary, we find that with our current algorithm it is better to fix one of the scattering parameters, and for the reasons explained in Section 3, we prefer to fix b . More sophisticated algorithms and scaling methods may give better images of A , b , and chromophore concentration; such algorithms are under investigation.

6. Generalization to Frequency- and Time-Domain Measurements

The multispectral method as formulated in Section 2 is applicable to frequency- and time-domain mea-

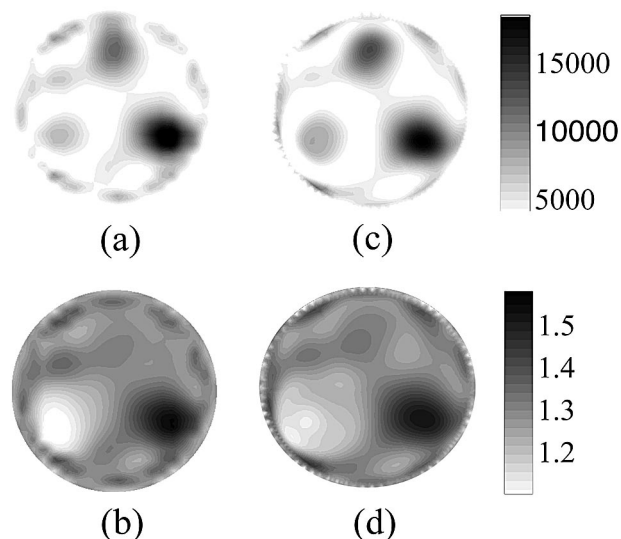


Fig. 10. The multispectral reconstruction of the target medium in Fig. 8, using the new set of variables (ζ , β), provides accurate A and b images as shown in (a) and (b), respectively. The A and b images displayed in (c) and (d), respectively, are reconstructed with the conventional method, i.e., fitting reconstructed $\mu_s'(\lambda)$ images at 15 wavelengths to the simplified Mie scattering form ($A\lambda^{-b}$).

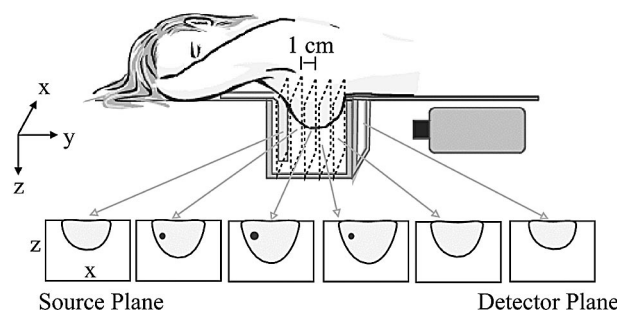


Fig. 11. Simplified schematic of the parallel-plate diffuse optical tomography instrument. The female subject lies in a prone position, and soft compression is applied with a source plate. Continuous-wave measurements are accomplished with a lens-coupled CCD in transmission mode. The orientation of image slices are shown beneath the instrument.

surements and will still be advantageous for reconstruction based on these data compared with traditional DOT image reconstructions.⁴¹ The multispectral approach improves frequency- and time-domain-based reconstructions because it effectively reduces the number of unknowns.

Our optimum wavelength analysis (Section 3), however, is based partially on nonuniqueness that arises when there is only one type of measurement available, i.e., either amplitude or phase. When the source-modulation frequency is high enough ($\omega \geq 50$ MHz) to produce phase changes larger than the phase noise, the residual norm R loses its importance. Therefore the wavelength sets 1 and 3 in Fig. 1 yield similar reconstructed images, whereas set 2 continues to show cross talk between absorption chromophore images; i.e., the choice of κ is still important in wavelength selection for frequency- and time-domain measurements. The importance of the residual norm, R , depends on the signal-to-noise ratio.

7. In Vivo Results

In this section we present preliminary *in vivo* 3D images obtained from a female subject with a cancerous breast lesion. We first give a brief description of our instrument and then outline some technical details in the data analysis and image reconstruction. We then compare images obtained with the two different methods: conventional DOT and multispectral DOT. We note, however, that such comparisons with *in vivo* data can never be fully conclusive, because we do not have *a priori* knowledge of the true physiological properties.

Figure 11 illustrates the basics of our instrument, a parallel-plate DOT system that has been characterized³ by use of various tissue phantoms and an *in vivo* healthy breast. The female subject lies in a prone position with both of her breasts inside the measurement box. The box is filled with a matching Intralipid fluid, and the breast is lightly compressed with a movable compression plate. Forty-five laser source fibers are located on this plate, forming a 9×5 regular grid. The cw and frequency-domain data are

acquired at four wavelengths (690, 750, 786, and 830 nm) in transmission mode (through a lens-coupled CCD) and in remission mode (through nine fibers located on the compression plate), respectively. 3D image reconstruction utilizes mainly 984 cw data points binned from the CCD. Frequency-domain data are utilized only in a preprocessing step to obtain a good initial guess for the breast and matching fluid optical properties.

In this study the total number of measurements used (including all wavelengths) was 84,524. A finite-element mesh⁴⁰ with 48071 nodes was constructed for the forward and inverse basis. A linear or nonlinear inversion in these large dimensions involving the Jacobian matrix with conventional DOT (single wavelength at a time) or multispectral DOT (multiple wavelengths simultaneously) requires approximately 15 and 120 Gbytes of memory, respectively. Both are well above the limit (3 Gbytes) of our current 32-bit computing platforms. Thus, for both conventional and multispectral (Subsection 2.B.2) DOT inversions, the gradient-based approach³⁶ was employed with spatially variant Tikhonov regularization.^{3,42} Recall that in conventional DOT, absorption and scattering values are reconstructed for each wavelength, and thus the total number of unknowns for each reconstruction node is 2 times the number of wavelengths. In the multispectral approach we have only four unknowns (HbO₂, HbR, H₂O, and A) at each node regardless of wavelength count.

We obtain reconstructed images of total hemoglobin concentration $\text{THC} = [\text{HbO}_2] + [\text{HbR}] \mu\text{M}$, blood oxygen saturation ($Y_T = 100 \times [\text{HbO}_2]/([\text{HbO}_2] + [\text{HbR}])$), water concentration and μ'_s at 786 nm. The lipid concentration was assumed to be 57% as reported in the literature.^{5,43,44} The scattering power

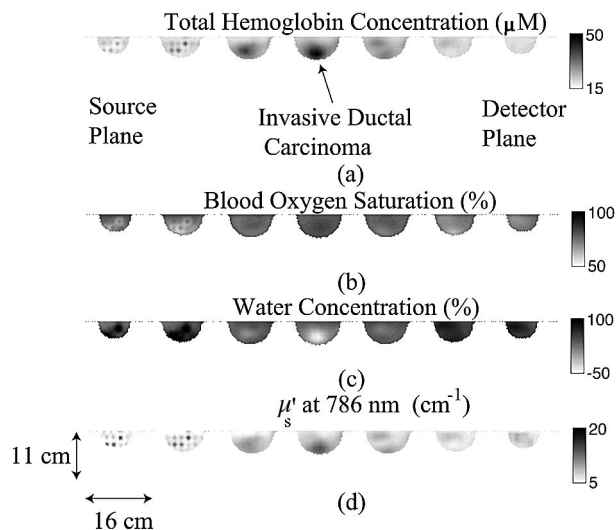


Fig. 12. Conventional DOT method was used to obtain (a) the reconstructed total hemoglobin concentration, (b) the blood oxygen saturation, (c) the water concentration, and (d) the scattering images of a subject with invasive ductal carcinoma near the nipple area. Note that the water concentration (c) drops to negative values.

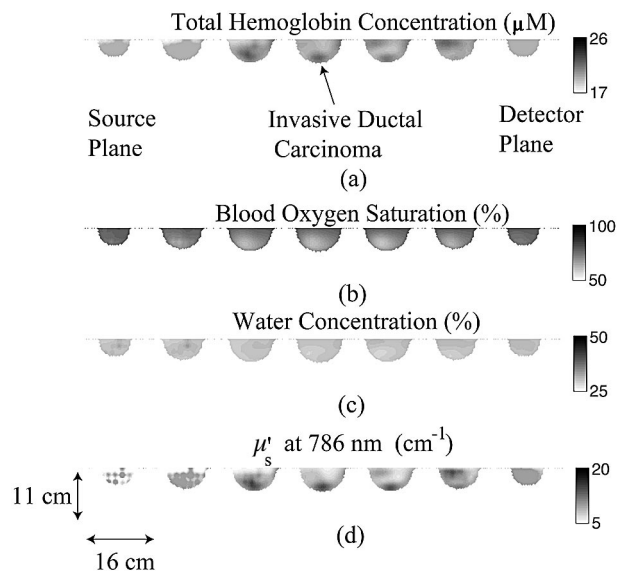


Fig. 13. (a) Total hemoglobin concentration, (b) blood oxygen saturation, (c) water concentration, and (d) scattering images of the same subject, reconstructed with the multispectral method. Reliable images were obtained compared with conventional DOT.

$b = 1.17$ was fixed according to bulk breast properties measured from frequency-domain data.

Figure 11 illustrates the orientation of the reconstructed images. The subject was a postmenopausal female with an invasive and *in situ* ductal carcinoma. Magnetic resonance imaging reported a mass of 2 cm in size in retroareolar (behind nipple) location where both DOT reconstruction methods indicate with high contrast in THC [Fig. 12(a) and Fig. 13(a)] and μ'_s [Fig. 12(d) and Fig. 13(d)] images. The two methods gave somewhat different images, however. The conventional DOT reconstruction showed negative water concentration at the cancer site [Fig. 12(c)], which was probably compensated by a false increase in THC [Fig. 12(a)]. The multispectral method, on the other hand, provided a more robust water concentration within the physiological range [Fig. 13(c)] even though the measurement wavelengths in our system do not fall into the optimum wavelength group; i.e., the measurement wavelength set has low $\kappa = 36.8$ and low $R = 0.05$ values. In total, the *in vivo* results provide evidence for the superiority of the multispectral DOT approach.

8. Summary

We have presented and tested multispectral DOT in detail. The *a priori* spectral model constrains the image reconstruction such that the number of unknowns stays constant even as the number of measurement wavelengths increases. We have shown that this technique can overcome the non-uniqueness problem observed in cw measurements, and we have developed a procedure to choose the best measurement wavelengths. The effects of different wavelength choices on image reconstruction were demonstrated with computer simulations and were

shown to be consistent with our theoretical expectations. We have discussed the optimum wavelengths for different absorption chromophores and wavelength combinations, and we have provided optimum wavelength distributions for typical experimental scenarios.

We have also shown that reliable separation of scattering prefactor (A) and scattering power (b) is possible with improvements in the scaling of the inverse problem. However, cross talk was observed in simulations in which the scattering prefactor (A), scattering power (b), and absorption chromophores were all allowed to vary. Finally, in our preliminary *in vivo* experiments we have compared the traditional DOT image reconstruction with the multispectral method. The former has shown comparatively improbable values for the water concentration that degrades the reliability of other chromophore concentration values.

We thank Joseph M. Giammarco for useful discussions and gratefully acknowledge funding from the National Institutes of Health grant 2-RO1-CA75124-04.

References

1. A. Yodh and B. Chance, "Spectroscopy and imaging with diffusing light," *Phys. Today*, **48**, 34–40 (1995).
2. A. G. Yodh and D. A. Boas, "Functional imaging with diffusing light," in *Biomedical Photonics* (CRC Press, Boca Raton, Fla., 2003), Chap. 21, pp. 1–45.
3. J. P. Culver, R. Choe, M. J. Holboke, L. Zubkov, T. Durduran, A. Slemple, V. Ntziachristos, D. N. Pattanayak, B. Chance, and A. G. Yodh, "Three-dimensional diffuse optical tomography in the parallel plane transmission geometry: evaluation of a hybrid frequency domain/continuous wave clinical system for breast imaging," *Med. Phys.* **30**, 235–247 (2003).
4. A. E. Cerussi, A. J. Berger, F. Bevilacqua, N. Shah, D. Jakubowski, J. Butler, R. F. Holcombe, and B. J. Tromberg, "Sources of absorption and scattering contrast for near-infrared optical mammography," *Acad. Radiol.* **8**, 211–218 (2001).
5. T. Durduran, R. Choe, J. P. Culver, L. Zubkov, M. J. Holboke, J. Giammarco, B. Chance, and A. G. Yodh, "Bulk optical properties of healthy female breast tissue," *Phys. Med. Biol.* **47**, 2847–2861 (2002).
6. T. O. McBride, B. W. Pogue, S. D. Jiang, and U. L. Osterberg, "A parallel-detection frequency-domain near-infrared tomography system for hemoglobin imaging of the breast *in vivo*," *Rev. Sci. Instrum.* **72**, 1817–1824 (2001).
7. V. Ntziachristos and B. Chance, "Probing physiology and molecular function using optical imaging: applications to breast cancer," *Breast Cancer Res. Treatment* **3**, 41–46 (2001).
8. V. Ntziachristos, A. G. Yodh, M. Schnall, and B. Chance, "Concurrent mri and diffuse optical tomography of breast after Indocyanine Green enhancement," *Proc. Natl. Acad. USA* **97**, 2767–2772 (2000).
9. B. W. Pogue, S. P. Poplack, T. O. McBride, W. A. Wells, K. S. Osterman, U. L. Osterberg, and K. D. Paulsen, "Quantitative hemoglobin tomography with diffuse near-infrared spectroscopy: pilot results in the breast," *Radiology* **218**, 261–266 (2001).
10. N. Shah, A. Cerussi, C. Eker, J. Espinoza, J. Butler, J. Fishkin, R. Hornung, and B. Tromberg, "Noninvasive functional optical spectroscopy of human breast tissue," *Proc. Natl. Acad. Sci. USA* **98**, 4420–4425 (2001).
11. D. A. Boas, D. H. Brooks, E. L. Miller, C. A. DiMarzio, M. Kilmer, R. J. Gaudette, and Q. Zhang, "Imaging the body with diffuse optical tomography," *IEEE Signal Process. Mag.* **18**, 57–75 (2001).
12. J. P. Culver, T. Durduran, D. Furuya, C. Cheung, J. H. Greenberg, and A. G. Yodh, "Diffuse optical tomography of cerebral blood flow, oxygenation and metabolism in rat during focal ischemia," *J. Cereb. Blood Flow Metab.* **23**, 911–924 (2003).
13. D. M. Hueber, M. A. Franceschini, H. Y. Ma, Q. Zhang, J. R. Ballesteros, S. Fantini, D. Wallace, V. Ntziachristos, and B. Chance, "Non-invasive and quantitative near-infrared haemoglobin spectrometry in the piglet brain during hypoxic stress, using a frequency-domain multidistance instrument," *Phys. Med. Biol.* **46**, 41–62 (2001).
14. B. W. Pogue and K. D. Paulsen, "High-resolution near-infrared tomographic imaging simulations of the rat cranium by use of a priori magnetic resonance imaging structural information," *Opt. Lett.* **23**, 1716–1718 (1998).
15. B. Chance, M. T. Dait, C. Zhang, T. Hamaoka, and F. Hagerman, "Recovery from exercise-induced desaturation in the quadriceps muscles of elite competitive rowers," *Am. J. Physiol.* **262**, C766–C775 (1992).
16. R. Belardinelli, T. J. Barstow, J. Porszasz, and K. Wasserman, "Skeletal muscle oxygenation during constant work rate exercise," *Med. Sci. Sports Exercise* **27**, 512–519 (1995).
17. K. W. Rundell, S. Nioka, and B. Chance, "Haemoglobin/myoglobin desaturation during speed skating," *Med. Sci. Sports. Exercise* **29**, 248–258 (1997).
18. H. Otaga, T. Yumoki, and T. Yano, "Effect of arm cranking on the NIRS determined blood volume and oxygenation of human inactive and exercising vastus lateralis muscle," *J. Appl. Physiol.* **86**, 191–195 (2002).
19. B. C. Wilson, M. S. Patterson, and S. T. Flock, "Indirect versus direct techniques for the measurement of the optical properties of tissues," *Photochem. Photobiol.* **46**, 601–608 (1987).
20. H. Wang, M. E. Putt, M. J. Emanuele, D. B. Shin, E. Glatstein, A. G. Yodh, and T. M. Busch, "Treatment-induced changes in tumor oxygenation predict photodynamic therapy outcome," *Cancer Res.* **64**, 7553–7561 (2004).
21. S. R. Arridge and W. R. B. Lionheart, "Nonuniqueness in diffusion-based optical tomography," *Opt. Lett.* **23**, 882–884 (1998).
22. Y. Pei, H. L. Graber, and R. L. Barbour, "Normalized-constraint algorithm for minimizing inter-parameter crosstalk in dc optical tomography," *Opt. Express* **9**, 97–109 (2001), <http://www.opticsexpress.org>.
23. H. L. Graber, Y. Pei, and R. L. Barbour, "Imaging of spatio-temporal coincident states by dc optical tomography," *IEEE Trans. Med. Imaging* **21**, 852–866 (2002).
24. C. H. Schmitz, M. Löcker, J. M. Lasker, A. H. Hielscher, and R. L. Barbour, "Instrumentation for fast functional optical tomography," *Rev. Sci. Instrum.* **73**, 429–439 (2002).
25. Y. Xu, X. Gu, T. Khan, and H. Jiang, "Absorption and scattering images of heterogenous scattering media can be simultaneously reconstructed by use of dc data," *Appl. Opt.* **41**, 5427–5437 (2002).
26. E. M. C. Hillman, "Experimental and theoretical investigations of near infrared tomographic imaging methods and clinical applications," Ph.D. thesis (University College London, 2002).
27. A. Corlu, T. Durduran, R. Choe, M. Schweiger, E. M. C. Hillman, S. R. Arridge, and A. G. Yodh, "Uniqueness and wavelength optimization in continuous-wave multispectral diffuse optical tomography," *Opt. Lett.* **28**, 2339–2341 (2003).
28. A. Li, Q. Zhang, J. P. Culver, E. L. Miller, and D. Boas, "Reconstructing chromosphere concentration images directly by continuous-wave diffuse optical tomography," *Opt. Lett.* **29**, 256–258 (2004).

29. T. Durduran, A. G. Yodh, B. Chance, and D. A. Boas, "Does the photon diffusion coefficient depend on absorption?" *J. Opt. Soc. Am. A*, **14**, 3358–3365 (1997).
30. D. J. Durian, "The diffusion coefficient depends on absorption," *Opt. Lett.* **23**, 1502–1504 (1998).
31. M. Schweiger, S. R. Arridge, M. Hiraoka, and D. T. Delpy, "The finite element model for the propagation of light in scattering media: boundary and source conditions," *Med. Phys.* **22**, 1779–1792 (1995).
32. F. Bevilacqua, A. J. Berger, A. E. Cerussi, D. Jakubowski, and B. J. Tromberg, "Broadband absorption spectroscopy in turbid media by combined frequency-domain and steady-state methods," *Appl. Opt.* **39**, 6498–6507 (2000).
33. J. R. Mourant, T. Fuselier, J. Boyer, T. M. Johnson, and I. J. Bigio, "Predictions and measurements of scattering and absorption over broad wavelength ranges in tissue phantoms," *Appl. Opt.* **36**, 949–957 (1997).
34. M. A. O'Leary, "Imaging with diffuse photon density waves," Ph.D. dissertation (University of Pennsylvania, Philadelphia, Pennsylvania, 1996).
35. S. R. Arridge, "Optical tomography in medical imaging," *Inverse Probl.* **15**, R41–R93 (1999).
36. S. R. Arridge and M. Schweiger, "A gradient-based optimization scheme for optical tomography," *Opt. Express* **2**, 213–226 (1998), <http://www.opticsexpress.org>.
37. S. J. Wright and J. Nocedal, eds., *Numerical Optimization* (Springer-Verlag, New York, 2000).
38. L. N. Trefethen and D. Bau, eds., *Numerical Linear Algebra* (Society for Industrial and Applied Mathematics, Philadelphia, 1997).
39. S. Prahl, "Optical properties spectra," retrieved 16 March 2003, <http://omlc.ogi.edu/spectra/index.html>, 2001.
40. S. R. Arridge, M. Schweiger, M. Hiraoka, and D. T. Delpy, "A finite element approach for modeling photon transport in tissue," *Med. Phys.* **20**, 299–309 (1993).
41. T. Durduran, "Non-invasive measurements of tissue hemodynamics with hybrid diffuse optical methods," Ph.D. dissertation (University of Pennsylvania, Philadelphia, 2004).
42. B. W. Pogue, T. O. McBride, J. Prewit, K. D. Osterberg, and U. L. Paulsen, "Spatially variant regularization improves diffuse optical tomography," *Appl. Opt.* **38**, 2950–2961 (1999).
43. D. R. White, H. Q. Woodward, and S. M. Hammond, "Average soft-tissue and bone models for use in radiation dosimetry," *Br. J. Radiol.* **60**, 907–913 (1987).
44. H. Q. Woodward and D. R. White, "The composition of body tissues," *Br. J. Radiol.* **59**, 1209–1219 (1986).